Colloidally engineered Pd and Pt catalysts distinguish surface- and vapor-mediated deactivation mechanisms

Jinwon Oh, ^{1,‡} Arik Beck, ^{2,‡} Emmett D. Goodman, ³ Luke T. Roling, ⁴ Anthony Boucly, ⁵ Luca Artiglia, ⁵ Frank Abild-Pedersen, ⁶ Jeroen A. van Bokhoven, ^{2,5,*} and Matteo Cargnello^{3,6,*}

¹ Department of Materials Science and Engineering, Stanford University, Stanford, California 94305,
United States

² Institute for Chemical and Bioengineering (ICB), ETH Zurich, Zurich 8093, Switzerland

³ Department of Chemical Engineering, Stanford University, Stanford, California 94305, United States

⁴ Department of Chemical and Biological Engineering, Iowa State University, Ames, Iowa 50011, United

States

⁵ Laboratory for Catalysis and Sustainable Chemistry (LSK), Paul Scherrer Institute, Villigen 5232, Switzerland

⁶ SUNCAT Center for Science and Catalysis, SLAC National Accelerator Laboratory, Menlo Park,

California 94025, United States

KEYWORDS

Sintering, Ostwald ripening, Deactivation, Supported catalysts, Colloidal nanocrystal

[‡]These authors contributed equally.

^{*}Corresponding authors: <u>jeroen.vanbokhoven@chem.ethz.ch</u>, <u>mcargnello@stanford.edu</u>

Abstract

Noble metal-based catalysts are ubiquitous because of their high activity and stability. However, they irreversibly deteriorate over time especially in high-temperature applications. In these conditions, sintering is the main reason for deactivation, and understanding how sintering occurs gives the opportunity to mitigate these detrimental processes. Previous studies successfully distinguished between two fundamental sintering modes, namely particle migration and coalescence (PMC) and Ostwald ripening (OR). However, differentiation between surface- and vapor-mediated Ostwald ripening processes has not been demonstrated yet, even though it is crucial information to tune metal/support interactions and stabilize catalysts. Here, we demonstrate that surface- and vapor-mediated ripening occur in two distinct regimes of temperature with some overlap using Pt and Pd catalysts prepared from colloidal nanocrystals as precursors. By either coimpregnating the two metal nanocrystals on the same grain of alumina support or by physically mixing powders of the two distinct metal catalysts, we tune the intermetal particle distance between nanometers and micrometers. We then use methane complete oxidation as a reporter reaction that occurs at higher rates on pure Pd and lower rates on alloyed Pd/Pt catalysts to trace the movement of Pt in the system. Aging the catalysts at different temperatures allows us to reveal that Pt initially sinters by surface-mediated ripening until ~750 °C, but at temperatures above 800 °C, vapor-mediated ripening by PtO₂ becomes the main sintering mechanism. This work demonstrates how colloidal catalysts allow unique insights into the working and deactivation mechanisms of supported systems.

Introduction

Deactivation of catalysts is a continuing problem in practical applications because replacement or regeneration of catalysts is expensive and time-consuming at industrial scale. Although the rate of deactivation depends on the reaction conditions, all catalysts unavoidably deactivate. There are various mechanisms of deactivation in heterogeneous catalysts related to chemical, mechanical, and thermal processes. Among them, sintering is a serious issue in the case of many metal-supported catalysts, because an excess amount of metal is used to compensate for deactivation by sintering. Sintering refers to the growth of metal nanoparticles by agglomeration and fusion at high temperature, which induces loss of active surface area. The driving force for nanoparticle sintering is the reduction of the overall chemical potential by loss of surface atoms. Although some methods are known to regenerate sintered catalysts, sintering is usually considered an irreversible deactivation process. Therefore, it is important to understand sintering mechanisms to minimize and/or avoid them.

There are two widely accepted sintering mechanisms: i) particle migration and coalescence (PMC), and ii) Ostwald (or atomic) ripening (OR). In the PMC mechanism, entire nanoparticles migrate on the support surface and merge to form larger particles. In OR, individual atoms in a nanoparticle transfer to other nanoparticles through the support surface (surface-mediated OR) or through the vapor phase (vapor-mediated OR). Previous studies successfully differentiated between PMC and OR. Particle size distribution (PSD) analysis after aging has been commonly used to determine the main sintering mechanism given that PMC and OR in principle result in different shapes of PSD.⁶ The emergence of particles smaller than those initially present in a sample is generally considered strong proof of OR-based sintering.⁷ The development of advanced *in situ* transmission electron microscopy (TEM) techniques allowed more clear differentiation

between PMC and OR by direct observations of nanoparticles during sintering phenomena.⁸ The movement, shrinkage and/or expansion of nanoparticles can be measured by imaging a certain region at different times. Movement followed by merging of nanoparticles is obvious evidence of PMC,⁹ whereas shrinking or expanding without particle mobility is evidence for OR. However, the distinction between surface- and vapor-mediated OR processes has not been clarified yet. The challenge is in the overlap in the mechanism between these two processes that makes it complicated to distinguish them.

Many studies clarified sintering mechanisms of palladium (Pd) and platinum (Pt) catalysts at various conditions using TEM.^{10–14} For example, Pt sinters mainly via OR in the presence of oxygen.¹⁵ Pd is relatively stable up to 800 °C, but it also sinters at high temperature via OR especially after its conversion from oxide to metallic Pd.⁷ However, as mentioned above, OR can occur via two different mechanisms, and further distinguishing between the two is important to design stable catalysts. Although there are numerous studies related to PMC and OR, differentiation between surface- and vapor-mediated ripening in Pt catalysts has not been reported. It has been hypothesized that PtO₂ is a mobile species formed under oxidizing conditions due to its volatile nature,¹⁵ which suggests that Pt sinters through vapor-mediated ripening. However, the contribution from surface-mediated ripening cannot be excluded. To precisely distinguish between vapor- and surface-mediated ripening through experiments, novel approaches are required.

Exploring factors other than reaction conditions is crucial to deeply understand fundamental aspects of sintering mechanisms. For instance, size and shape of nanoparticles affect the degree of sintering, because they modify the chemical potential of surface atoms.⁵ Therefore, to understand the impact of reaction conditions alone on sintering, it is desirable to use nanoparticles which have uniform size and shape to fairly study mechanisms of sintering. Colloidal nanoparticles emerged

as precursors for supported catalysts that facilitate fundamental studies of catalytic phenomena because size and morphology of pre-formed nanoparticles can be tuned and controlled to a fine extent. Support materials can also affect sintering of catalysts. The rate of sintering depends on the adhesion energy of active metal to the support. In addition, sintering of the support can induce encapsulation of active metal and deactivate catalysts. Therefore, support properties should be thoroughly acknowledged to properly understand the sintering mechanisms of active materials.

In this work, controlled catalysts prepared from colloidal Pd and Pt nanoparticles were synthesized with control over the spatial location of the two phases. Commercial alumina was used as the support because of its ubiquitous use in practical applications, and because it is recognized as one the best supports for Pd in methane complete oxidation. By either co-impregnating particles on the same support grain or by physically mixing grains of the two distinct metal catalysts, the intermetal particle distance could be tuned between nanometers (co-impregnated sample) and micrometers (physically mixed) without changing the nature of either metal phase (i.e. size, composition, metal/support interactions). In the co-impregnated catalyst, both surface- and vapormediated sintering can occur, because the two metals are deposited on the same grain. However, we hypothesize that surface-mediated ripening cannot occur in the case of the physically mixed catalyst due to the high barrier for mobile species to cross support grains, and vapor-mediated ripening is the only viable sintering mechanism. Furthermore, previous work found that alloying Pt with Pd significantly decreases the activity of Pd catalysts for methane complete oxidation.¹⁹ Based on this knowledge, catalytic activity for methane complete oxidation is used as a reporter to evaluate the degree of Pt moving and alloying with Pd, and thus sintering. By aging the catalyst systems at different temperatures and comparing their degree of deactivation, we reveal that Pt initially sinters by surface-mediated ripening and, at a certain temperature under our conditions,

vapor-mediated ripening by PtO₂ starts to occur. In this way, we directly demonstrate how ripening mechanisms occur in relevant catalysts and conditions that will inform researchers on the design of sinter-resistant catalysts.

Experimental Section

Synthesis of colloidal nanoparticles

All syntheses were performed using standard Schlenk techniques according to previous work.²⁰ For Pd particles, 152.3 mg of palladium (II) acetylacetonate (Pd(acac)₂, 35% Pd, Acros Organics), 9 mL of 1-octadecene (ODE, 90%, Acros Organics), 11 mL of 1-tetradecene (TDE, 94%, Alfa Aesar) and 3.4 mL of 1-oleylamine (OLAM, 70%, Sigma-Aldrich) were mixed in a three-neck flask. For Pt particles, 157.3 mg of platinum (II) acetylacetonate (Pt(acac)₂, 98%, Acros Organics), 1.3 mL of OLAM, 5.1 mL of oleic acid (OLAC, 90%, Sigma-Aldrich) and 20 mL of trioctylamine (TOA, 98%, Sigma-Aldrich) were mixed in a three-neck flask. The mixture was evacuated at room temperature for 15 min. Next, an appropriate amount (1.14 mL for Pd and 0.1 mL for Pt) of trioctylphosphine (TOP, 97%, Aldrich) was added, and the mixture was degassed for an additional 30 min at 50 °C for Pd and 120 °C for Pt. The reaction flask was then flushed with nitrogen and heated quickly (~40 °C min⁻¹) to the reaction temperature (245 °C for Pd and 250 °C for Pt). After 15 min for Pd and 30 min for Pt of reaction at the reaction temperature under magnetic stirring, the solution was quickly cooled to room temperature. The particles were isolated by precipitation with the addition of isopropanol, ethanol, methanol, and acetone, then centrifugation (838 rad s⁻¹, 3 min). They were then redissolved in 5 mL of hexanes. This procedure was repeated three times for Pd and two times for Pt and the particles finally redissolved in hexanes for further use.

Synthesis of supported catalysts

Alumina was prepared by calcining Puralox TH100/150 (obtained from Sasol) at 900 °C for 24 h using heating and cooling ramps of 3 °C min⁻¹ in static air. To obtain a uniform distribution of nanoparticles on the support, alumina was surface-functionalized with 3-amino-1,2-propanediol

(APD, 98%, Sigma-Aldrich) by following a previous study.²⁰ Prior to impregnation, metal concentrations of synthesized colloidal nanoparticle solutions were determined by thermogravimetric analysis (TGA). A nanoparticle solution was added dropwise into an aluminum TGA pan, which was heated on a hot plate at ~100 °C and 200 µL of nanoparticle solution was added. This pan was then further heated in the TGA system in flowing air up to 500 °C, and held until a steady mass was reached, indicating complete removal of solvents and organics. Dividing this final mass by the volume of solution added gave the metal concentration. Then, an appropriate volume of nanoparticle solution was diluted in hexanes and added to a dispersion of ~2 g of APDfunctionalized alumina stirred in 40 mL of ethanol-toluene mixture (4 mL of ethanol and 36 mL of toluene). For the co-impregnated sample, Pd and Pt nanoparticles solutions were first mixed, and this solution of mixed NPs was added to the support dispersion. After 1 h, the solid was recovered by centrifugation (838 rad s⁻¹, 1 min) and dried at 60 °C overnight. The dried supported catalysts were calcined at 450 °C for 30 min in static air to remove residual surfactants. Before catalytic tests, all samples were sieved below 180 µm grain size, fast-treated at 700 °C for 30 s in a furnace to remove ligands from synthesis as previously described, 21 then sieved again below 180 µm grain size.

Characterization

Low-magnification TEM was performed on a Tecnai system operating at 200 kV. Scanning TEM (STEM) micrographs were acquired by using a JEOL Grand ARM 300 aberration-corrected microscope operating at 300 kV. The metal composition of single nanoparticles in the catalyst were determined using Energy dispersive X-ray spectroscopy (EDS) mapping of catalyst grains. EDS maps were recorded by two detectors in STEM mode of the JEOL Grand ARM 300. The data

Spectra of individual metal particles were created by integration of all pixels assigned to the particle. Quantification of the metal content of the particles was only performed when the resulting spectra showed a reasonable signal-to-noise ratio. This analysis may introduce a bias towards larger particles, since the spectral quality of small nanoparticles (<3 nm) did not allow precise quantification and are thus not represented in Figure 5.

The sample for XPS measurement was prepared in the form of a pellet using a gold mesh as a support. Around 15 mg of catalysts was used and pressed for 1 min under 1 ton. The pellet was then fixed on the manipulator and introduced in the chamber. The chamber was filled with a gas mixture composed of 1 mbar O₂ and N₂ at a ratio of 1:4 with the temperature raised at 50 °C to avoid carbon accumulation and diminish charging effect.

The XPS measurements were done at the X07DB *in situ* spectroscopy beamline at the Swiss Light Source (SLS) using the solid-gas interface experimental chamber. One Kinetic Energy (KE=530 eV, considering the static charging displayed by the samples during measurements) was used, with the Pd 3d / Pt 4d measured at hv=890 eV and the O 1s measured at hv=1090 eV. Al 2p, acquired as a reference peak, was measured at all energies as well at hv=620 eV to have it at same KE as the other two core level peaks. The binding energy scales of O 1s and Pd 3d were aligned based on Al 2p, whose binding energy was fixed at 74.5 eV. For physical mixture samples, a second Kinetic Energy was investigated (KE=730 eV) with the Pd 3d / Pt 4d measured at hv=1090 eV and O 1s measured at hv=1290 eV. The Al 2p reference peak was measured at all energies and at hv=820 eV, to have it at same KE as the other core level peaks. Collecting all the photoemission peaks at the same KE ensures that the spectral information comes from the same escape depth. Measuring the spectra in a 1 mbar gas environment causes scattering of the photoelectrons in the gas phase. This in turn influences the intensity of the spectra, thus the signal to noise ratio (S/N).

In order to improve the S/N, the kinetic energy of the electron analyzer was swept 120 times across the Pd 3d region reported in Figure 5i-5k. The deconvolutions of photoemission spectra were done upon subtraction of a Shirley background and using Gaussian-shaped peaks. The spin orbit splitting of Pd 3d was set to 5.3 eV. The fitting parameters used (peaks positions, shape and full width at half maximum) are based on previous reports obtained on palladium foil and supported palladium nanoparticles.^{24,25}

X-ray fluorescence data was collected using a Spectro Xepos HE XRF Spectrometer. The spectrometer is equipped with a Solid-State Detector (SSD) and samples are run at 4 different energies.

Catalytic characterization

The catalytic tests were carried out using a fixed-bed flow reactor. For the reaction, the same amount of Pd was used for measuring the catalytic activity of Pd/Al₂O₃, co-impregnated Pd/Pt/Al₂O₃ catalyst and physical mixture Pd/Al₂O₃+Pt/Al₂O₃ catalysts. 100 mg of catalysts for Pd/Al₂O₃, 200 mg of catalysts for co-impregnated catalyst and physical mixture were used, to begin with the same catalytic activity for all of them (Pt does not contribute appreciably to the overall activity). The catalysts were loaded into a U-shaped quartz microreactor with an internal diameter of 1 cm to give a bed length of about 1 cm. The catalysts were packed between acidwashed silica sand layers, which were used for preventing displacement of the catalyst powder and for preheating the reactant gases. The reactor was heated by a Micromeritics Eurotherm 2416 furnace, and the temperature was recorded by a K-type thermocouple inserted inside the catalytic bed. All pre-treatments and catalytic reactions were conducted at atmospheric pressure.

Prior to the catalytic reaction, an oxidative pretreatment (45 mL min⁻¹ of 5 vol. % O₂/Ar) at 300 °C for 30 min was carried out to remove residual surface compounds. Next, the reactant mixture was introduced. The reactant mixture composition was controlled by varying the flow rates of 5 vol. % CH₄/Ar, 5 vol. % O₂/Ar, and Ar (all certified mixtures with purity >99.999% from Airgas). The reaction mixture consisted of 0.25 vol. % CH₄ and 4.0 vol. % O₂ with balance Ar at a flow rate of 50 mL min⁻¹ at 300 °C. After 45 min of reaction, the reactant mixture was removed, and the catalyst was ramped to the target aging temperature (700, 750, 800, 850 °C) at 20 °C min⁻¹. The catalyst was aged at a flow rate of 50 mL min⁻¹ in 5 vol. % O₂/Ar or Ar for 60 min, and ramped down to 300 °C at 20 °C min⁻¹, at which point the reaction mixture was reintroduced to the reactor for 1 h. Degree of deactivation was assessed by comparing the conversion before and after the aging procedure.

Electronic Structure Calculations

All calculations were performed using periodic density functional theory (DFT) as implemented in the Quantum ESPRESSO package²⁶ using ultra-soft pseudopotentials²⁷ and the BEEF-vdW functional.²⁸ A plane-wave cutoff of 500 eV and density cutoff of 5000 eV were used.

The optimized lattice parameters of PdO were calculated to be a = 3.125 Å and c = 5.455 Å, in reasonable agreement with the experimental parameters of 3.043 Å and 5.336 Å, respectively.²⁹ Within this computational framework, we calculate a formation enthalpy of -0.91 eV for PdO at 0 K, which is in good agreement with the experimental value of -0.97 eV.³⁰ The PdO(100)-O slab was constructed with a 2x2 surface unit cell and seven metal layers (14 total metal atoms); the bottom four layers were fixed at the bulk-optimized positions, and all other atoms were allowed to freely relax. The PdO(101) slab was constructed with a 2x2 surface unit cell and four metal layers

(16 total metal atoms); the top two layers were allowed to fully relax. The surface Brillouin zones of the PdO models were sampled with a 4x4x1 Monkhorst-Pack k-point mesh.³¹ The Pt catalyst model was constructed with an optimized lattice constant of 4.016 Å, which compares with the experimental value of 3.942 Å. The Pt(111) slab was constructed with a 2x2 surface unit cell and six metal layers; the top two layers were allowed to fully relax. The surface Brillouin zone was sampled with a 6x6x1 k-point mesh. At least 15 Å of vacuum separated successive slabs for all models. The dipole correction to the total energy was included for slab calculations.³²

All geometry optimizations were performed until forces on atoms were less than 0.02 eV/Å. Free energies of adsorption are calculated as $\Delta G = \Delta E + \Delta Z P E - T \Delta S$, where G is the free energy, E is the total energy, ZPE is the zero-point energy correction, T is the absolute temperature, and S is the entropy. ZPE and S were calculated from the vibrational frequencies of adsorbates, calculated within the harmonic approximation.

Results and discussion

In this work, we utilized well-defined catalysts prepared from colloidal Pd and Pt nanoparticle precursors and controlled the distance between them to differentiate surface- and vapor-mediated Ostwald ripening (OR). We hypothesized that catalysts with precise distributions of metal nanoparticles among grains would lead to clarify their contributions. Specifically, we assumed that Pd and Pt particles dispersed onto different support grains could interact with each other only through vapor-mediated sintering processes. Instead, samples where both particles were present on the same support grain could also interact through surface-mediated processes (Figure 1). It has previously been demonstrated that Pd and Pt sinter by OR, not by particle migration and coalescence, in conditions very similar to what used in this work. ^{13,14} In this way, we could distinguish between surface-mediated and vapor-mediated OR.

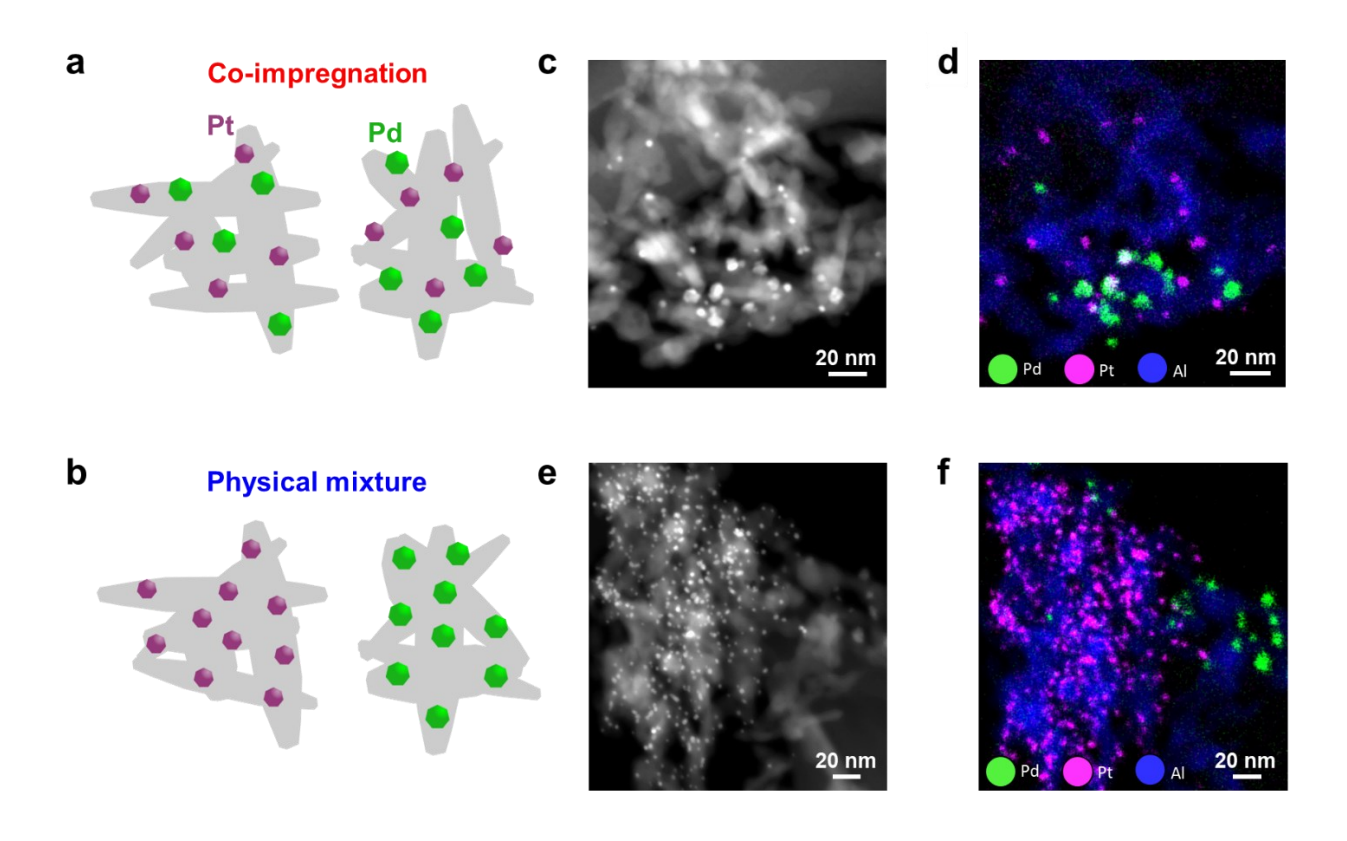


Figure 1. (a) and (b) Schematic representations of the nature of co-impregnated and physical mixture catalyst grains showing the physical intimacy and separation, respectively, of the Pt and Pd nanoparticles in the two types of catalysts. Representative HAADF-STEM images ((c) and (e)) and corresponding EDS maps ((d) and (f)) of co-impregnated Pd/Pt/Al₂O₃ catalyst and physical mixture Pd/Al₂O₃+Pt/Al₂O₃ catalysts, respectively.

Pd and Pt nanoparticles with different average diameters of 3.7 ± 0.4 and 2.0 ± 0.5 nm (to aid the characterization), respectively, were prepared (Figure S1 in the Supporting Information). The nanoparticles were then impregnated on a commercial alumina support that was surfacefunctionalized to improve the uniform distribution of nanoparticles.²⁰ Two different processes were used for the impregnation to obtain particle distributions as depicted in Figure 1a and 1b. In the co-impregnated catalyst (Pt/Pd/Al₂O₃), colloidal Pd and Pt nanoparticles were added to the support mixture during the same impregnation step so that both metals were present at the same time across all support grains. In contrast, Pd/Al₂O₃ and Pt/Al₂O₃ catalysts were prepared separately and mixed in powder form in the sample labeled as physical mixture to keep grains containing only Pd or only Pt particles separate. The Pd and Pt weight loadings were 0.40 wt. % and 1.3 wt. %, respectively, as measured by X-ray fluorescence (XRF) (Figure S2 in the Supporting Information). Representative high-angle annular dark-field scanning transmission electron microscopy (HAADF-STEM) images and energy-dispersive X-ray spectroscopy (EDS) maps demonstrated that Pd and Pt nanoparticles were co-located on support grains in the coimpregnated catalyst (Figure 1c and 1d). Instead, characterization of the physical mixture sample clearly showed the separate distribution of the two metal nanoparticle populations (Figure 1e and 1f).

It is known that Pt sinters at lower temperature compared to Pd under oxidizing conditions.³³ It is also known that addition of Pt deactivates Pd catalysts for methane complete oxidation in the absence of large volumes of steam.¹⁹ We therefore considered using the activity of Pd for methane complete oxidation to decipher whether Pt is sintering and causing a decreased reactivity. To assess the feasibility of this method, we performed first-principles density functional theory (DFT) calculations to understand the deactivation mechanism induced by Pt on Pd, with specific focus on the process by which Pt migrates and affects the reactivity of PdO particles. For simplicity and consistency with previous computational work, 15 the migration of Pt at 600 °C is modelled in the vapor phase via formation of PtO₂, but this does not exclude the surface migration of similarly reactive and volatile species. We also note that previous comparisons of vapor- and surfacemediated mechanisms were made for SiO₂, and it is therefore possible that Al₂O₃ could facilitate a support-mediated ripening mechanism as well.² As calculated in that work, such vapor-phase migration is relevant at temperatures as low as 400 °C at the experimental pressures used (~40 mbar). To investigate the adsorption of PtO2 and other relevant surface intermediates on Pt and PdO surfaces, we performed calculations on PdO(100)-O (denoting the oxygenated surface termination) and PdO(101) (stoichiometric termination) surfaces (Figure S3a and S3b in the Supporting Information), which are the most stable surface terminations under relevant methane oxidation conditions.³⁴ We also performed calculations on a Pt(111) surface model to represent the Pt catalyst (Figure S3c in the Supporting Information), considering that Pt is metallic and only presenting a layer of chemisorbed oxygen under our experimental conditions. All calculated free energies are presented at 600 °C to verify whether the reaction between PtO2 and PdO can occur even though formation and emission of volatile PtO₂ species may be kinetically slow and be the limiting step.

We calculated that PtO₂ adsorption is unfavorable at 600 °C on a pristine PdO(100)-O surface $(\Delta G_{ads} = +0.69 \text{ eV})$, in stark contrast to its favorable adsorption on Pt(111) $(\Delta G_{ads} = -1.04 \text{ eV})$. This observation suggests that there is no obvious thermodynamic driving force for the migration of PtO₂ from pure Pt nanoparticles to pristine PdO. However, the methane complete oxidation cycle on PdO results in the consumption of surface oxygen, yielding oxygen vacancies. Substoichiometric PdO_x phases are also likely to form vacancies in the absence of methane. This surface oxygen would generally be replenished by adsorption of gas phase O₂ from the reaction environment. The adsorption of a full O₂ molecule in a vacancy is unfavorable ($\Delta G_{ads} = +0.93 \text{ eV}$) due to the formation of a weakly-bound surface O atom in addition to the O atom used to replenish the surface vacancy. This weakly-bound atom ($\Delta G_{ads} = +1.90 \text{ eV}$, relative to ½ $O_2(g)$) can readily recombine with other surface O and desorb to yield a clean, replenished PdO(100)-O surface with the vacancy filled by the remaining O atom ($\Delta G_{ads} = -0.97 \text{ eV}$). In the conditions of methane complete oxidation, vapor-phase PtO₂ forms and competes with O₂ for the available oxygen vacancies in the PdO(100)-O surface. In fact, the adsorption of PtO₂ in a surface vacancy ($\Delta G_{ads} =$ -0.63 eV) is far stronger than adsorption of O₂, primarily due to the stability of the newly formed surface PtO relative to that of atomic O (Figure 2a.). This process establishes a vacancy-mediated mechanism by which Pt can migrate from Pt nanoparticles to the PdO(100)-O surface through a PtO₂(g) intermediate; we note that this migration from Pt(111) is thermodynamically uphill by 0.41 eV.

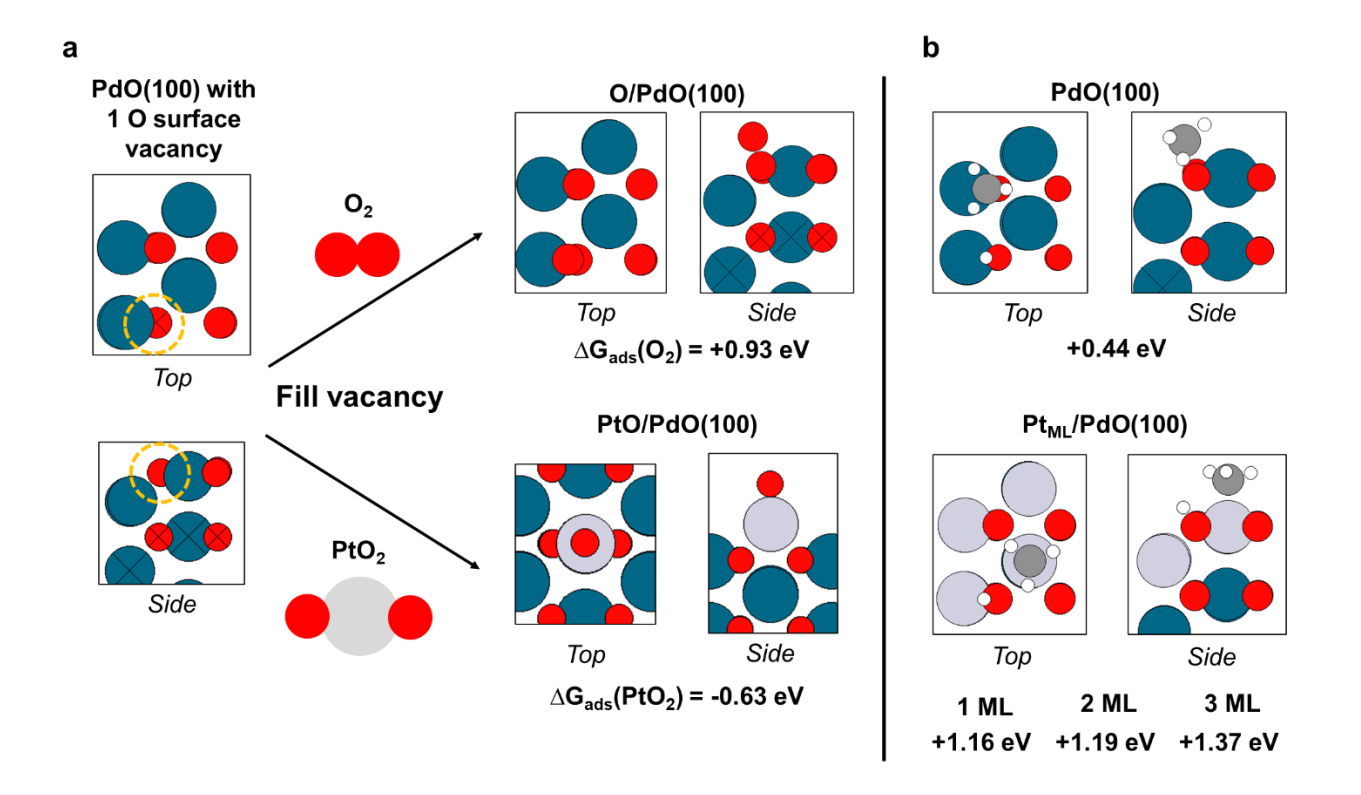


Figure 2. (a) DFT calculation of the adsorption free energies of O₂ and PtO₂ on the surface of PdO(100) with an oxygen surface vacancy (marked with an orange circle). (b) CH₄ dissociation energy on the pure PdO(100) surface and the Pt_{ML}/PdO(100). All values were calculated at 600 °C and 1 atm. Atoms are colored as follows: red (O), white (H), blue (Pd), grey (Pt).

Once one PtO₂ adsorbs in a vacancy (yielding a surface PtO), it can serve as a nucleation site for the adsorption of subsequent PtO₂ molecules. Adsorption of a second PtO₂ (yielding a PtO-PtO₂ surface complex) is much more favorable than the first ($\Delta G_{ads} = -1.10 \text{ eV}$) and does not require the presence of a surface oxygen vacancy. PtO₂ continues to favorably adsorb and, through the release of O₂(g), a continuous PtO surface layer with a 1:1 Pt:O ratio is formed, which our calculations show is most favorable under the operating conditions. This ultimately suggests the formation of at least a stable PtO monolayer (PtO-ML) on the PdO(100)-O surface. Relative to bulk Pt and gas-

phase O_2 , this monolayer adsorbs with a free energy of +0.05 eV per PtO. We also evaluated the energetics of forming additional complete PtO overlayers on PdO(100)-O, and while the formation of the first layer was mildly endergonic, the formation of the second and third monolayer was more unfavorable with $\Delta G = +0.29$ eV and +0.34 eV per PtO, respectively. This further observation suggests that there is no driving force for continued growth of PtO overlayers on the PdO(100)-O particle surface, although there may still be a thermodynamic gain for removing undercoordinated Pt atoms, which are less stable than bulk Pt atoms.

The trend of increasing free energy with number of layers also suggests that the sequential formation of PtO layers is a self-limiting process: since each layer binds more weakly than the previous layer, there will be a thermodynamic preference to form complete layers on all PdO particles before forming multiple layers on a few particles, assuming that stable PtO monolayers are indeed formed. We further note that the formation of O-vacancies in PtO overlayers is more difficult than on the pure PdO surface: ΔG_{ads} of ½ O₂ is -1.41 eV, -1.30 eV, and -1.27 eV in vacancy sites of the 1 ML, 2 ML, and 3ML PtO surfaces, compared to just -0.97 eV in a vacancy of the PdO(100)-O surface. Together, these results imply that Pt may distribute rather uniformly across the surfaces of Pd particles during the sintering process.

We performed a similar analysis for vacancy-mediated PtO₂ migration on the PdO(101) surface. In this case, O₂ ($\Delta G_{ads} = +0.31$ eV) and PtO₂ ($\Delta G_{ads} = -0.75$ eV) adsorb more strongly in an O-vacancy than on PdO(100)-O. However, formation of a PtO-ML structure is less favorable on Pd(101) ($\Delta G = +0.33$ eV per PtO), which is less stable by 0.28 eV than the monolayer on PdO(100)-O. Since PdO(100)-O is the more stable facet and the energetics of PtO overlayer formation are more favorable on PdO(100)-O, this process (although feasible) is likely less significant on PdO(101).

We finally calculate energetics for the overall transformation of the segregated Pt and PdO nanoparticles to form alloyed Pt-Pd bimetallic catalysts. At 600 °C, we find that the bulk Pt + PdO system is preferred over Pt + Pd + $\frac{1}{2}$ O₂ by 0.01 eV per metal atom, validating our assumption that the Pd catalyst is still primarily in its oxide form at that elevated temperature. As mentioned previously, the formation of PtO overlayers is overall unfavorable relative to bulk Pt + O₂(g). However, subsequent alloying of the Pd with Pt should release O₂ to form a more stable bimetallic alloy than either of the original Pt or PdO components. Depending on the specific Pt/Pd ratio of the final particles, we calculate that the Pd/Pt alloy (+ released O₂) is more stable than isolated Pt + PdO by 0.012 – 0.015 eV per metal atom at 600 °C. This contribution is favorable even without considering further contributions from mixing entropy, which can be estimated according to a mean-field approximation as an additional 0.04 - 0.05 eV per metal atom, depending on the Pt/Pd ratio.³⁵ Although the difference in calculated energies might be in the error range of DFT energy calculation, our estimation that the Pd/Pt alloy should be preferred over mixed oxide at the condition of this study is consistent with a previous in-depth study of the stability of mixed Pd-Pt oxides using DFT calculations,³⁶ and it is also consistent with our experimental particle characterization.Click or tap here to enter text.

We also briefly investigated the methane complete oxidation energetics by calculating the free energy change of methane dissociation, which is an indicator of the relative rates of methane activation, on PdO(100)-O and PtO-modified PdO(100)-O (PtO-ML). Although a detailed investigation of the reaction energetics, including the nature of the active site on these catalysts, is beyond the scope of this current work, a comparison of the methane dissociation energies between PdO and PtO-modified surfaces can offer a first-order explanation of the potential activity (while noting that neither metallic Pt or Pd have particularly favorable methane oxidation chemistry at

low temperatures). Methane dissociation (to form adsorbed CH₃ + H) is 0.72 eV more favorable at 600 °C on the pure PdO(100)-O surface than on the PtO-ML surface, suggesting that the PdO surface will have substantially lower activation energy barriers (via well-known correlations between activation energy and thermochemistry)³⁷ for this reaction than Pt-modified surfaces (Figure 2b). This calculation clearly demonstrates that the PtO-modified surface is far less active than PdO, explaining why addition of Pt to Pd leads to decreased rates for methane complete oxidation. Overall, our computational work demonstrates that PtO₂ can migrate and alloy with Pd particles leading to some form of atom trapping as described in recent work³⁸ and that leads to decreased activity for methane complete oxidation. Therefore, this reaction can be used as a tool to study the degree of sintering of Pt affecting Pd catalysts.

We set to study the activity and stability of the Pd and Pt catalysts to correlate their structure with deactivation. The protocol to measure catalyst deactivation included a measurement of the initial catalytic activity of the sample at 300 °C, an aging step in either oxidative conditions or pure Ar (as a control condition) at four different temperatures (700 °C, 750 °C, 800 °C, 850 °C) for 1 hour, and then another measurement of catalytic activity at 300 °C (Figure 3a). Degree of deactivation was assessed by comparing the conversion before and after the aging procedure (Equation S1 in the Supporting Information). Therefore, stable catalysts would show no decrease in activity before and after the aging step; however, if sintering affects Pt and Pd distributions in the samples leading to alloying of the two into the less active bimetallic phase, a decrease in activity is expected. All samples were prepared from the same batch of Pd and Pt nanoparticles to avoid batch-to-batch variations. Additionally, the amount of Pd was kept constant in all the three types of catalysts that were prepared (Pd/Al₂O₃ catalyst, co-impregnated Pd/Pt/Al₂O₃ catalyst, and physically mixed Pd/Al₂O₃+Pt/Al₂O₃ catalyst), and the co-impregnated and physically mixed

samples had the same amount of Pt nanoparticles. As predicted from previous work, the Pd/Al₂O₃ catalyst showed much higher catalytic activity compared to the Pt/Al₂O₃ catalyst (Figure 3b),¹⁹ thus the contribution of Pt to the sample's overall activity at 300 °C can be considered negligible. Therefore, all three catalysts showed a similar level of CH₄ conversion (~70%) at 300 °C at the beginning of the experiments (Figure 3c).

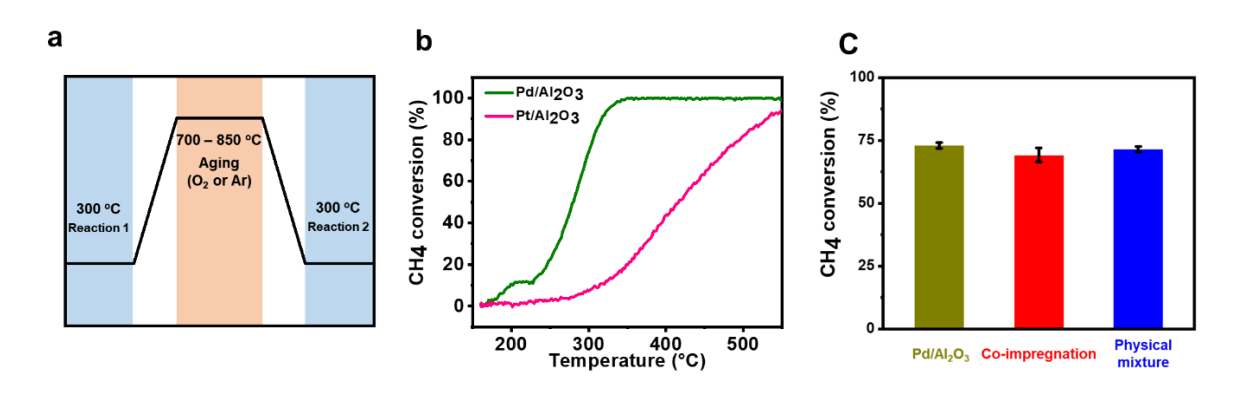


Figure 3. (a) The protocol to measure catalyst deactivation. (b) Light off-curves of Pd/Al₂O₃ (green) and Pt/Al₂O₃ (pink) catalysts. (c) Initial CH₄ conversion at 300 °C of as-synthesized Pd/Al₂O₃ (green), co-impregnated Pd/Pt/Al₂O₃ catalyst (red), physical mixture Pd/Al₂O₃+Pt/Al₂O₃ catalysts (blue).

The conversion after aging varied with different sample configurations. We reported the degree of deactivation and methane oxidation conversion recorded for different samples against the aging temperature used in the protocol explained above (Figure 4 and Table S1 in the Supporting Information). Physically mixed Pd/Al₂O₃+Pt/Al₂O₃ catalysts and Pd/Al₂O₃ catalyst showed a similar degree of deactivation after the aging at temperatures of 700 °C and 750 °C (Pd/Al₂O₃ catalyst: 6% and 17%, Pd/Al₂O₃+Pt/Al₂O₃ catalysts: 6% and 18%). On the other hand, deactivation of the co-impregnated Pd/Pt/Al₂O₃ catalyst reached 23% and 53% at 700 °C and 750 °C. The

noticeable difference in catalyst deactivation following these aging treatments suggests that the close interaction between Pd and Pt in the co-impregnated catalyst is the reason for the more marked deactivation than in the physical mixture. Given that the Pd/Al₂O₃ catalyst does not deactivate to such a large extent, the deactivation in the co-impregnated sample must be because of Pt sintering, leading to the lower activity expected for alloys. Furthermore, since the two metals are impregnated on different support grains in the physical mixture, surface-mediated ripening cannot occur. Therefore, we can hypothesize that the deactivation observed in the co-impregnated catalyst is due to surface-mediated ripening, because Pd/Pt sintering did not occur in the physical mixture according to the data that we are presenting below.

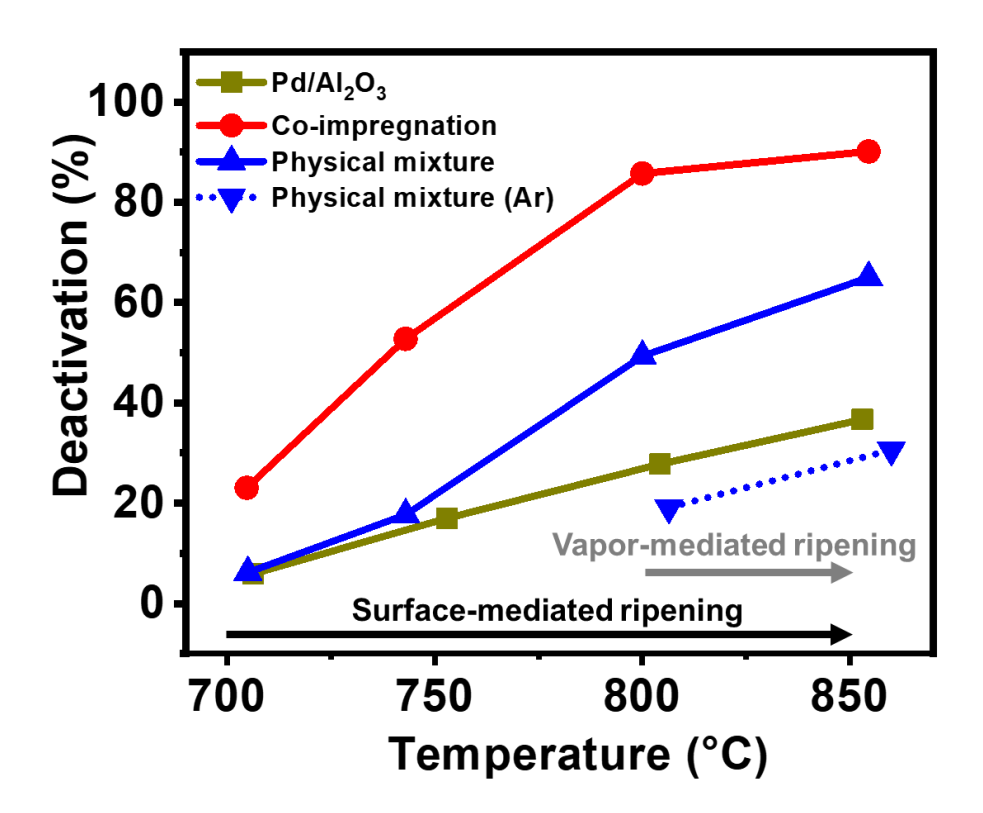


Figure 4. The degree of catalyst deactivation (in percentage) reported as a function of aging temperature for Pd/Al₂O₃ (green squares), co-impregnated Pd/Pt/Al₂O₃ catalyst (red circles),

physical mixture Pd/Al₂O₃+Pt/Al₂O₃ catalysts (upward-pointing blue triangles) aged under O₂, and physical mixture Pd/Al₂O₃+Pt/Al₂O₃ catalysts aged under Ar (downward-pointing blue triangles).

At aging temperatures of 800°C and above, the physical mixture started to deviate significantly from the deactivation curve of the Pd/Al₂O₃ catalyst. This deviation suggests the emergence of sintering between Pd and Pt in the physical mixture that is distinct from the deactivation processes occurring to the Pd/Al₂O₃ catalyst. Although vapor-mediated ripening is expected to be the main sintering mechanism in the physical mixture, the possibility of long-distance surface-mediated ripening (grain to grain) at high temperatures can also be considered. In fact, we cannot discard that the increase in temperature allowed the system to overcome the energy barrier for the process in which monomers traverse different alumina grains. To verify the main sintering mechanism, the physical mixture was aged at 800 °C and 850 °C under pure Ar. The degree of deactivation significantly decreased under these conditions. This result suggests that sintering did not actively occur in the absence of oxygen. Therefore, it is likely that some form of platinum oxide that is known to have high volatility is responsible for ripening at high temperatures either in the vapor phase or through surface transport above 800 °C.

Additionally, the deactivation values for the physical mixture sample at the higher temperatures of aging are still smaller than the corresponding values for the co-impregnated sample (~60% and ~90% at 850 °C, respectively). This observation suggests that different mechanisms for sintering occur in the co-impregnated and physical mixture samples. For the co-impregnated sample, both surface- and vapor-mediated ripening occurred. Vapor-mediated ripening most likely contributed in the physical mixture. Based on these observations, we postulate that the difference in the deactivation values between the co-impregnated and physical mixture at high temperatures mainly comes from the effect of surface-mediated ripening that had occurred in the former but not in the

latter. We also postulate that longer aging times at the higher temperature would result in the two systems to get comparable deactivation values, since eventually the two catalysts would thermodynamically end in the same final state.

We primarily investigated particle size distribution of aged samples using STEM (Figure S4 in the Supporting Information). The average particle diameter significantly increased in coimpregnated Pd/Pt/Al₂O₃ catalyst that were aged at 700 °C and kept increasing at higher aging temperatures. However, the size increase in the physical mixture Pd/Al₂O₃+Pt/Al₂O₃ catalysts was not significant until the aging temperature of 750 °C. After aging at 850 °C, both samples showed similar average particle size. To further understand and explain the structural and compositional changes occurring to the catalysts, they were characterized more in detail after aging treatments at 700 and 850 °C under oxygen using EDS mapping and synchrotron-based x-ray photoelectron spectroscopy (XPS). EDS maps of the co-impregnated Pd/Pt/Al₂O₃ catalyst aged at 700 °C revealed that Pd and Pt signals overlapped (Figure 5a). Quantification of the Pd and Pt signal at the single particle level was performed and plotted against the particle size, demonstrating that smaller particles were mostly composed of Pd, whereas larger particles contained a larger fraction of Pt (Figure 5b). The Pt content increased at increasing particle diameter, indicating that Pt-based species are the mobile species that react with PdO nanoparticles. In contrast, for the physical mixture Pd/Al₂O₃+Pt/Al₂O₃ catalysts aged at 700 °C, Pd and Pt signals were found to come from separate regions of the catalyst (Figure 5c). The particle composition was mainly dominated by small, mostly Pt particles and larger, mostly Pd particles (Figure 5d). However, a large fraction of nanoparticles with a diameter smaller than 10 nm were found in TEM analysis (Figure S5 in the Supporting Information). This observation suggests that some small Pd-rich particles escaped the EDS analysis. Additionally, the compositional profiles measured by EDS in the physical mixture

sample indicated a lower degree of mixing between Pd and Pt compared to the co-impregnated sample, suggesting that sintering phenomena are mostly limited to Pd-Pd and Pt-Pt interactions. Small particles in this sample showed the presence of a small amount of Pd in mostly Pt particles (Figure 5d). This result suggests that some degree of Pd sintering is possible followed by Pt migration, or that some level of Pd migration to Pt exists at this low temperature, in agreement with our previous work on alumina-supported Pd catalysts.² Similar EDS maps and signal distributions were instead found for both catalysts aged at 850 °C (Figure 5e and 5g), with overlapping Pd and Pt signals. Individual particle distributions also indicated that Pd and Pt signals were homogeneously distributed among particles of different sizes (Figure 5f and 5h). These observations indicate that drastic sintering had occurred in both catalysts at this high aging temperature, in line with previous reports.^{38,39} The average Pd atomic composition of catalysts aged at 850 °C was ~25% and ~20% for the co-impregnated and physically mixed samples, respectively. Both values are below the expected bulk metal sample atomic composition of ~36% Pd. This result means that presumably a fraction of Pd-rich particles was not captured by the EDS analysis, which are most likely small nanoparticles that contribute too little to the signal used for the analysis.

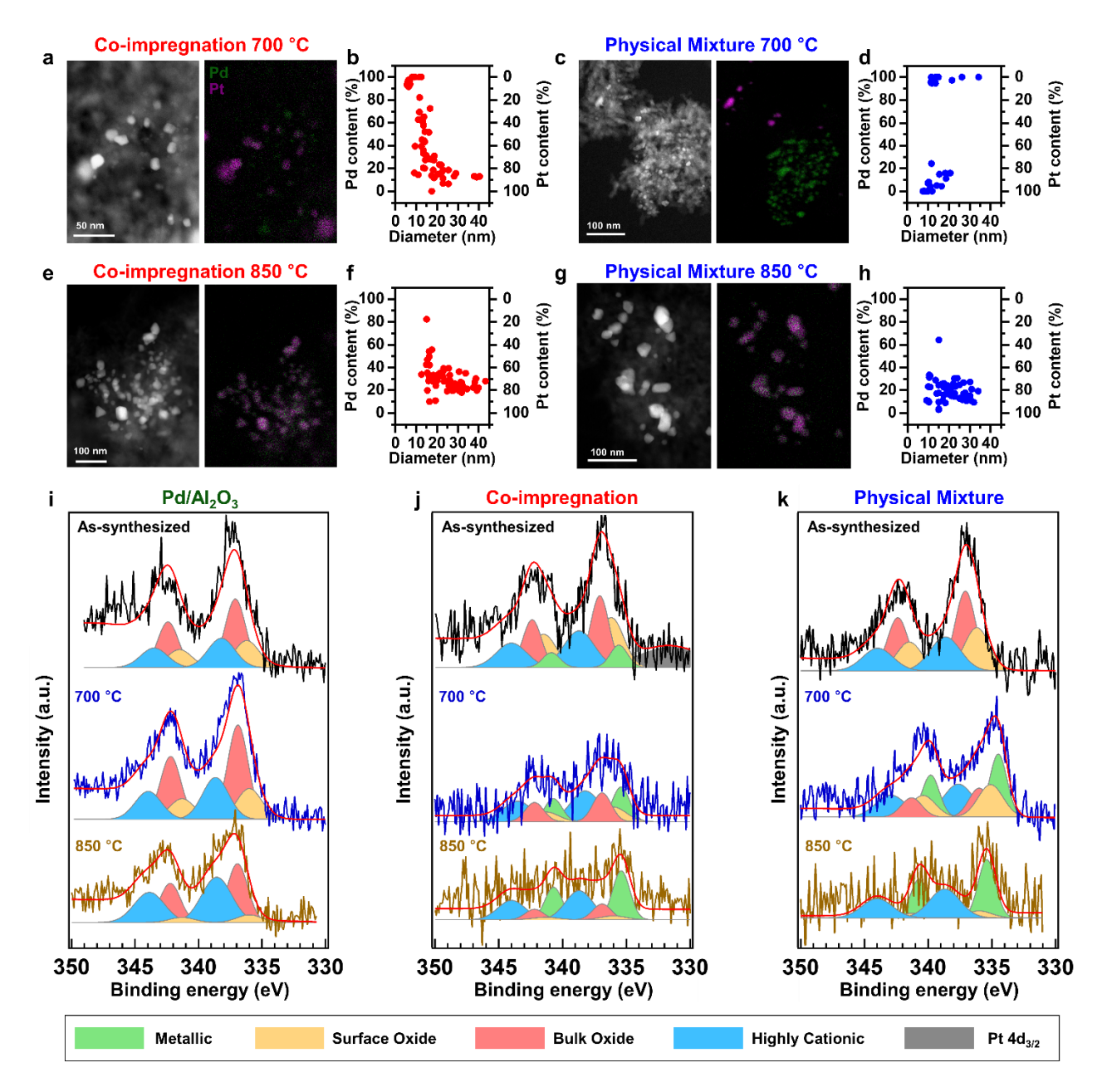


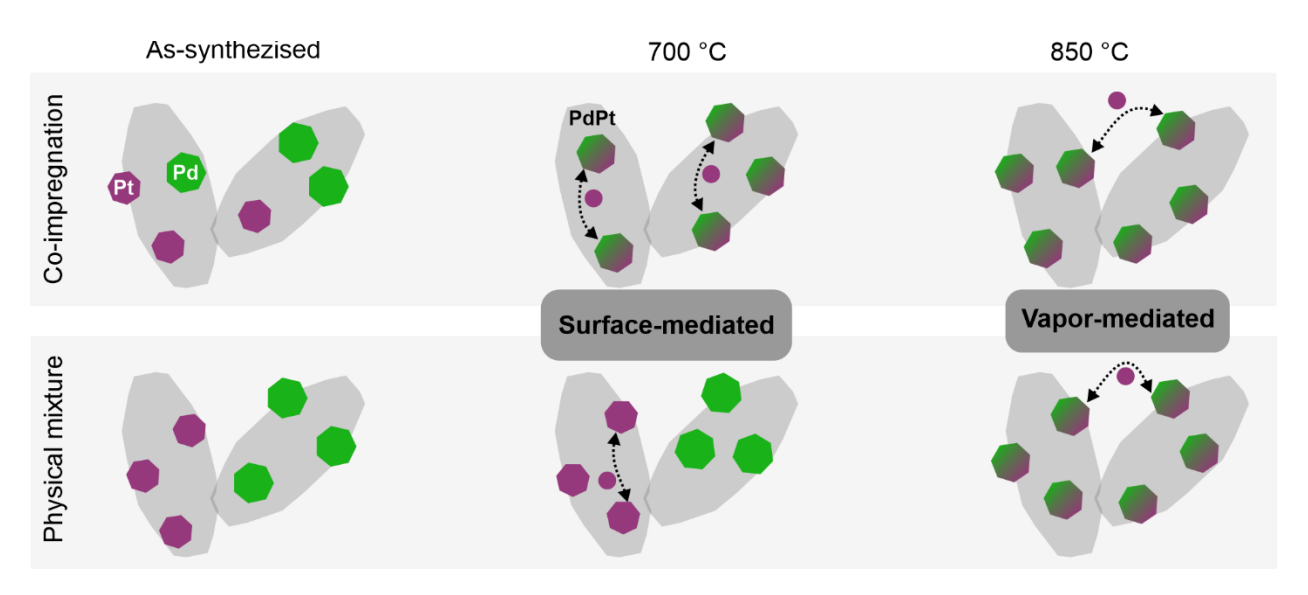
Figure 5. HAADF-STEM images and corresponding EDS maps (Pd: Green, Pt: Pink) of aged co-impregnated Pd/Pt/Al₂O₃ catalyst ((a): aged at 700 °C, (e): aged at 850 °C) and aged physical mixture Pd/Al₂O₃+Pt/Al₂O₃ catalysts ((c): aged at 700 °C, (g): aged at 850 °C). Pd and Pt contents versus particle diameter plots of aged co-impregnated catalyst ((b): aged at 700 °C, (f): aged at 850 °C) and aged physical mixture catalysts ((d): aged at 700 °C, (h): aged at 850 °C). XPS

spectrum of Pd/Al₂O₃ (i), co-impregnated catalyst (j), physical mixture catalysts (k) before (black: as-synthesized) and after aging treatment (blue: aged at 700 °C, green: aged at 850 °C).

Previous studies reported the formation of bimetallic, alloyed Pd/Pt nanoparticles when a physical mixture of supported catalysts containing these metals was exposed to air, with PdO being converted into metallic Pd. 38,40 Our DFT calculations also demonstrate that Pt addition to PdO leads to its favorable reduction to metallic state (Figure 2a). XPS was used to explore oxidation state changes after aging. Pd 3d photoemission spectra of as-synthesized and aged Pd/Al₂O₃, coimpregnated Pd/Pt/Al₂O₃ catalyst, and the physical mixture Pd/Al₂O₃+Pt/Al₂O₃ catalysts showed a complex pattern containing contributions from multiple species (Figure 5i, 5j, and 5k). The signal was deconvoluted into four components that were attributed to metallic, surface oxide, bulk oxide, and highly cationic Pd species.^{24,25} This latter species is commonly observed in low loading catalysts and has been attributed to Pd atoms strongly interacting with the support.^{2,25} In Pd/Al₂O₃ catalyst, only oxidized Pd species were detected in both fresh and aged samples (Figure 5i). In contrast, signals related to all the Pd species were found even in the initial co-impregnated catalyst (Figure 5j). This result is likely due to a small amount of sintering between Pd and Pt occurring during the catalyst preparation and ligand removal process at 700 °C in static air (see Experimental Section for details). In this same catalyst, the Pd/Al ratio decreased after the 700 °C aging and the fraction of metallic state species increased, with a corresponding decrease of the oxide species signals (See Figure S6 and Table S2 in the Supporting Information). After aging the coimpregnated catalyst at 850 °C, metallic Pd signal was dominant in addition to that of highly cationic Pd species. The as-synthesized physical mixture catalyst showed a similar spectrum composition as that of Pd/Al₂O₃ catalyst, with no metallic Pd signal that could be discerned (Figure

5k). However, after aging at 700 °C, signal related to metallic Pd species was found with a concurrent decrease in that of oxidized states (See Table S2 in the Supporting Information). In addition, the Pd/Al ratio also decreased which indicated the loss of surface Pd atoms (See Figure S6 in the Supporting Information). We measured high kinetic energy (730 eV) XPS to use a larger probing depth of aged nanoparticles, and evaluated the ratio between Pd and Pt. The Pd/Pt ratio decreased in surface-sensitive measurements after aging, but it increased in bulk sensitive measurement (See Figure S7 in the Supporting Information). This result suggests that Pt atoms covered the surface of Pd nanoparticles. We observed sintered nanoparticles that consisted of both Pd and Pt from the EDS map of physical mixture catalysts aged at 700 °C (Figure 5c and 5d) and the XPS results also showed alloying of Pd and Pt at this aging temperature. Given that the physical mixture aged at 700 °C showed a similar degree of deactivation compared to the Pd/Al₂O₃ catalyst (Figure 4), we hypothesize that a small amount of sintering between Pd and Pt does not significantly decrease the activity for methane complete oxidation. Metallic Pd was the main species in the spectrum of the physical mixture aged at 850 °C, which was like that of the coimpregnated catalyst aged at the same temperature (See Table S2 in the Supporting Information). In summary, combining EDS and XPS results with catalytic results, we propose the following sintering mechanisms and structures (Scheme 1). In the case of the co-impregnated Pd/Pt/Al₂O₃ catalyst, Pt sintered via surface-mediated ripening at 700 °C and reacted with Pd to form bimetallic, alloyed nanoparticles. At increasing aging temperatures, vapor-mediated ripening takes also place, leading to an overall homogeneous distribution of Pd and Pt in larger particles. In the physical mixture Pd/Al₂O₃+Pt/Al₂O₃ catalysts, less sintering is observed after the 700 °C aging process because of the barrier for Pt to sinter via surface-mediated processes and react with Pd on different alumina grains. At higher temperature, however, vapor-mediated ripening occurs and most of the

particles are converted into bimetallic, alloyed nanoparticles. Thus, the final state of both catalysts is very similar after the 850 °C aging, but the mechanisms by which the aging leads to sintering is different due to the different metal particle spatial distribution that was created through the colloidal approach.



Scheme 1. Sintering mechanisms and proposed structures of co-impregnated Pd/Pt/Al₂O₃ catalyst and physical mixture Pd/Al₂O₃ +Pt/Al₂O₃ catalysts.

Conclusions

In this work, we differentiated surface- and vapor-mediated ripening by using colloidally engineered catalysts. Two catalysts (co-impregnated Pd/Pt/Al₂O₃ catalyst and physical mixture Pd/Al₂O₃+Pt/Al₂O₃ catalysts) which have different distances between Pd and Pt nanoparticles were studied. Methane complete oxidation was used as a probe reaction because alloying of Pd and Pt significantly deactivates Pd catalysts based on our DFT calculation. The catalysts were aged at different temperature and their activity decrease was compared with Pd/Al₂O₃ to track the sintering between Pd and Pt. By comparing the degree of deactivation after aging and confirming

element distributions of nanoparticles using EDS maps, we found Pt initially sintered with Pd by surface-mediated ripening. However, at the aging temperature above 800 °C, vapor-mediated ripening started to occur by a Pt oxide form. With these results, this work provides a fundamental knowledge in sintering mechanisms of Pt and Pd, specifically by distinguishing surface- and vapor-mediated ripening.

AUTHOR INFORMATION

Corresponding Author

* Jeroen A. van Bokhoven - Institute for Chemical and Bioengineering (ICB), ETH Zurich, Zurich 8093, Switzerland; Laboratory for Catalysis and Sustainable Chemistry (LSK), Paul Scherrer Institute, Villigen 5232, Switzerland; Email: jeroen.vanbokhoven@chem.ethz.ch

* Matteo Cargnello - Department of Chemical Engineering, Stanford University, Stanford, California 94305, United States; SUNCAT Center for Science and Catalysis, SLAC National Accelerator Laboratory, Menlo Park, California 94025, United States; Email: mcargnello@stanford.edu

Author Contributions

The manuscript was written through contributions of all authors. All authors have given approval to the final version of the manuscript. ‡These authors contributed equally.

Notes

The authors declare no competing financial interest.

ASSOCIATED CONTENT

Supporting Information

TEM images and particle size distributions of as-synthesized Pd and Pt nanoparticles, XRF, Surface models for DFT calculation, Particle size analysis on aged catalysts, TEM images and particle size distribution of the physical mixture catalyst aged at 700 °C, Evolution of the Pd/Al ratio for the co-impregnated and physical mixture catalysts, Evolution of Pd/Pt ratio for the physical mixture catalysts, Equation for degree of deactivation, Table of methane oxidation conversion of as-synthesized and aged catalysts, Table of the Pd 3d signal percentage coming from different Pd species. This information is available free of charge on the ACS Publications website.

ACKNOWLEDGMENTS

This work was mainly supported by the National Science Foundation under grant 1956300 (J.O.). Additional support was provided by the US Department of Energy, Chemical Sciences, Geosciences, and Biosciences Division of the Office of Basic Energy Sciences, via the grant DE-AC02-76SF00515 to the SUNCAT Center for Interface Science and Catalysis. Part of this work was performed at the Stanford Nano Shared Facilities (SNSF), supported by the National Science Foundation under award ECCS-2026822. A.B. and J.A.vB. thank the SNSF project 200021_178943 for funding of the research. We thank Frank Krumeich for the TEM support and the Scientific Center for Optical and Electron Microscopy (ScopeM) at ETH Zurich for the access to TEM.

REFERENCES

- (1) Argyle, M. D.; Bartholomew, C. H. Heterogeneous Catalyst Deactivation and Regeneration: A Review. *Catalysts* **2015**, *5* (1), 145–269.
- (2) Goodman, E. D.; Johnston-Peck, A. C.; Dietze, E. M.; Wrasman, C. J.; Hoffman, A. S.; Abild-Pedersen, F.; Bare, S. R.; Plessow, P. N.; Cargnello, M. Catalyst Deactivation via Decomposition into Single Atoms and the Role of Metal Loading. *Nat. Catal.* **2019**, *2* (9), 748–755.
- (3) Hansen, T. W.; Delariva, A. T.; Challa, S. R.; Datye, A. K. Sintering of Catalytic Nanoparticles: Particle Migration or Ostwald Ripening? *Acc. Chem. Res.* **2013**, *46* (8), 1720–1730.
- (4) Goodman, E. D.; Schwalbe, J. A.; Cargnello, M. Mechanistic Understanding and the Rational Design of Sinter- Resistant Heterogeneous Catalysts. *ACS Catal.* **2017**, *7* (10), 7156–7173.
- (5) Dai, Y.; Lu, P.; Cao, Z.; Campbell, C. T.; Xia, Y. The Physical Chemistry and Materials Science behind Sinter-Resistant Catalysts. *Chem. Soc. Rev.* **2018**, *47*, 4314–4331.
- (6) Datye, A. K.; Xu, Q.; Kharas, K. C.; McCarty, J. M. Particle Size Distributions in Heterogeneous Catalysts: What Do They Tell Us about the Sintering Mechanism? *Catal. Today* **2006**, *111*, 59–67.
- (7) Goodman, E. D.; Carlson, E. Z.; Dietze, E. M.; Tahsini, N.; Johnson, A.; Aitbekova, A.; Nguyen Taylor, T.; Plessow, P. N.; Cargnello, M. Size-Controlled Nanocrystals Reveal Spatial Dependence and Severity of Nanoparticle Coalescence and Ostwald Ripening in Sintering Phenomena. *Nanoscale* **2021**, *13* (2), 930–938.

- (8) Delariva, A. T.; Hansen, T. W.; Challa, S. R.; Datye, A. K. In Situ Transmission Electron Microscopy of Catalyst Sintering. *J. Catal.* **2013**, *308*, 291–305.
- (9) Frey, H.; Beck, A.; Huang, X.; van Bokhoven, J. A.; Willinger, M. G. Dynamic Interplay between Metal Nanoparticles and Oxide Support under Redox Conditions. *Science* **2022**, *376* (6596), 982–987.
- (10) Zhang, S.; Cargnello, M.; Cai, W.; Murray, C. B.; Graham, G. W.; Pan, X. Revealing Particle Growth Mechanisms by Combining High-Surface-Area Catalysts Made with Monodisperse Particles and Electron Microscopy Conducted at Atmospheric Pressure. *J. Catal.* **2016**, *337*, 240–247.
- (11) Simonsen, S. B.; Chorkendorff, I.; Dahl, S.; Skoglundh, M.; Sehested, J.; Helveg, S. Ostwald Ripening in a Pt/SiO2 Model Catalyst Studied by in Situ TEM. *J. Catal.* **2011**, *281* (1), 147–155.
- (12) Yin, P.; Hu, S.; Qian, K.; Wei, Z.; Zhang, L. le; Lin, Y.; Huang, W.; Xiong, H.; Li, W. X.; Liang, H. W. Quantification of Critical Particle Distance for Mitigating Catalyst Sintering. *Nat. Commun.* **2021**, *12* (1). No.4865
- (13) Simonsen, S. B.; Chorkendorff, I.; Dahl, S.; Skoglundh, M.; Helveg, S. Coarsening of Pd Nanoparticles in an Oxidizing Atmosphere Studied by in Situ TEM. *Surf. Sci.* **2016**, *648*, 278–283.
- (14) Simonsen, S. B.; Chorkendorff, I.; Dahl, S.; Skoglundh, M.; Sehested, J.; Helveg, S. Direct Observations of Oxygen-Induced Platinum Nanoparticle Ripening Studied by in Situ TEM. *J. Am. Chem. Soc.* **2010**, *132* (23), 7968–7975.

- (15) Plessow, P. N.; Abild-Pedersen, F. Sintering of Pt Nanoparticles via Volatile PtO2: Simulation and Comparison with Experiments. *ACS Catal.* **2016**, *6* (10), 7098–7108.
- (16) Cargnello, M.; Fornasiero, P.; Gorte, R. J. Playing with Structures at the Nanoscale: Designing Catalysts by Manipulation of Clusters and Nanocrystals as Building Blocks. *ChemPhysChem* **2013**, *14* (17), 3869–3877.
- (17) Campbell, C. T. The Energetics of Supported Metal Nanoparticles: Relationships to Sintering Rates and Catalytic Activity. *Acc. Chem. Res.* **2013**, *46* (8), 1712–1719.
- (18) Xu, Q.; Kharas, K. C.; Croley, B. J.; Datye, A. K. The Sintering of Supported Pd Automotive Catalysts. *ChemCatChem* **2011**, *3* (6), 1004–1014.
- (19) Goodman, E. D.; Dai, S.; Yang, A. C.; Wrasman, C. J.; Gallo, A.; Bare, S. R.; Hoffman, A. S.; Jaramillo, T. F.; Graham, G. W.; Pan, X.; Cargnello, M. Uniform Pt/Pd Bimetallic Nanocrystals Demonstrate Platinum Effect on Palladium Methane Combustion Activity and Stability. *ACS Catal.* **2017**, *7* (7), 4372–4380.
- (20) Kao, K.; Yang, A.; Huang, W.; Zhou, C.; Goodman, E. D.; Holm, A.; Frank, C. W.; Cargnello, M. A General Approach for Monolayer Adsorption of High Weight Loadings of Uniform Nanocrystals on Oxide Supports. *Angew. Chem.* **2021**, *133* (14), 8050–8058.
- (21) Cargnello, M.; Chen, C.; Diroll, B. T.; Doan-Nguyen, V. V. T.; Gorte, R. J.; Murray, C. B. Efficient Removal of Organic Ligands from Supported Nanocrystals by Fast Thermal Annealing Enables Catalytic Studies on Well-Defined Active Phases. *J. Am. Chem. Soc.* **2015**, *137* (21), 6906–6911.

- (22) Roy, K.; Artiglia, L.; van Bokhoven, J. A. Ambient Pressure Photoelectron Spectroscopy: Opportunities in Catalysis from Solids to Liquids and Introducing Time Resolution. *ChemCatChem* **2018**, *10* (4), 666–682.
- (23) Orlando, F.; Waldner, A.; Bartels-Rausch, T.; Birrer, M.; Kato, S.; Lee, M.-T.; Proff, C.; Huthwelker, T.; Kleibert, A.; van Bokhoven, J.; Ammann, M. The Environmental Photochemistry of Oxide Surfaces and the Nature of Frozen Salt Solutions: A New in Situ XPS Approach. *Top. Catal.* **2016**, *59* (5–7), 591–604.
- (24) Li, X.; Wang, X.; Roy, K.; van Bokhoven, J. A.; Artiglia, L. Role of Water on the Structure of Palladium for Complete Oxidation of Methane. *ACS Catal.* **2020**, *10* (10), 5783–5792.
- (25) Boucly, A.; Artiglia, L.; Roger, M.; Zabilskiy, M.; Beck, A.; Ferri, D.; van Bokhoven, J. A. Water Inhibition and Role of Palladium Adatoms on Pd/Al2O3 Catalysts during Methane Oxidation. *Appl. Surf. Sci.* **2022**, 154927.
- (26) Giannozzi, P.; Baroni, S.; Bonini, N.; Calandra, M.; Car, R.; Cavazzoni, C.; Ceresoli, D.; Chiarotti, G. L.; Cococcioni, M.; Dabo, I.; Dal Corso, A.; de Gironcoli, S.; Fabris, S.; Fratesi, G.; Gebauer, R.; Gerstmann, U.; Gougoussis, C.; Kokalj, A.; Lazzeri, M.; Martin-Samos, L.; Marzari, N.; Mauri, F.; Mazzarello, R.; Paolini, S.; Pasquarello, A.; Paulatto, L.; Sbraccia, C.; Scandolo, S.; Sclauzero, G.; Seitsonen, A. P.; Smogunov, A.; Umari, P.; Wentzcovitch, R. M. QUANTUM ESPRESSO: A Modular and Open-Source Software Project for Quantum Simulations of Materials. *J. Phys.: Condens. Matter* **2009**, *21* (39), 395502.
- (27) Vanderbilt, D. Soft Self-Consistent Pseudopotentials in a Generalized Eigenvalue Formalism. *Phys. Rev. B* **1990**, *41* (11), 7892–7895.

- (28) Wellendorff, J.; Lundgaard, K. T.; Møgelhøj, A.; Petzold, V.; Landis, D. D.; Nørskov, J. K.; Bligaard, T.; Jacobsen, K. W. Density Functionals for Surface Science: Exchange-Correlation Model Development with Bayesian Error Estimation. *Phys. Rev. B* **2012**, *85* (23), 235149.
- (29) Rogers, D. B.; Shannon, R. D.; Gillson, J. L. Crystal Growth and Semiconductivity of Palladium Oxide. *J. Solid State Chem.* **1971**, *3* (2), 314–316.
- (30) CRC Handbook of Chemistry and Physics, 95th Edition; Haynes, W. M., Lide, D. R., Bruno, T. J., Eds.; CRC Press, **2014**; 12-15-12-18.
- (31) Monkhorst, H. J.; Pack, J. D. Special Points for Brillouin-Zone Integrations. *Phys. Rev. B* **1976**, *13* (12), 5188–5192.
- (32) Bengtsson, L. Dipole Correction for Surface Supercell Calculations. *Phys. Rev. B* 1999, 59(19), 12301–12304.
- (33) Johns, T. R.; Gaudet, J. R.; Peterson, E. J.; Miller, J. T.; Stach, E. A.; Kim, C. H.; Balogh, M. P.; Datye, A. K. Microstructure of Bimetallic Pt-Pd Catalysts under Oxidizing Conditions. *ChemCatChem* **2013**, *5* (9), 2636–2645.
- (34) Rogal, J.; Reuter, K.; Scheffler, M. Thermodynamic Stability of PdO Surfaces. *Phys. Rev.* B **2004**, 69 (7), 075421.
- (35) Neugebauer, J.; van de Walle, C. G. Electronic Structure and Phase Stability of GaAs_{1-x}N_x Alloys. *Phys. Rev. B* **1995**, *51* (16), 10568–10571.
- (36) Dianat, A.; Seriani, N.; Bobeth, M.; Pompe, W.; Ciacchi, L. C. DFT Study of the Thermodynamic Stability of Pd–Pt Bulk Oxide Phases. *J. Phys. Chem. C* **2008**, *112* (35), 13623–13628.

- (37) Xing, B.; Pang, X.-Y.; Wang, G.-C. C–H Bond Activation of Methane on Clean and Oxygen Pre-Covered Metals: A Systematic Theoretical Study. *J. Catal.* **2011**, *282* (1), 74–82.
- (38) Carrillo, C.; Johns, T. R.; Xiong, H.; Delariva, A.; Challa, S. R.; Goeke, R. S.; Artyushkova, K.; Li, W.; Kim, C. H.; Datye, A. K. Trapping of Mobile Pt Species by PdO Nanoparticles under Oxidizing Conditions. *J. Phys. Chem. Lett.* **2014**, *5* (12), 2089–2093.
- (39) Graham, G. W.; Jen, H.-W.; Ezekoye, O.; Kudla, R. J.; Chun, W.; Pan, X. Q.; McCabe, R. W. Effect of Alloy Composition on Dispersion Stability and Catalytic Activity for NO Oxidation over Alumina-Supported Pt–Pd Catalysts. *Catal. Lett.* **2007**, *116* (1–2), 1–8.
- (40) Xiong, H.; Peterson, E.; Qi, G.; Datye, A. K. Trapping Mobile Pt Species by PdO in Diesel Oxidation Catalysts: Smaller Is Better. Catal. Today *2016*, 272 (1), 80–86.

Table of Contents Graphic

